Modeling and kinetic Monte Carlo simulations of the metallographic etching process of second phase particles

Ihor Sobchenko, Dietmar Baither, Rudolf Reichelt, Eckhard Nembach

Modeling and kinetic Monte Carlo simulations of the metallographic etching process of second phase particles

Journal:	*Philosophical Magazine & Philosophical Magazine Letters*
Manuscript ID:	TPHM-09-Apr-0140.R1
Journal Selection:	Philosophical Magazine
Date Submitted by the Author:	20-Jul-2009
Complete List of Authors:	Sobchenko, Ihor; Universitaetsklinikum, Institut fuer Medizinische Physik und Biophysik Baither, Dietmar; University of Muenster, Institut fuer Materialphysik Reichelt, Rudolf; Universitaetsklinikum, Institut fuer Medizinische Physik und Biophysik Nembach, Eckhard; University of Muenster, Institut fuer Materialphysik
Keywords:	atomic force microscopy, chemical etching, high-resolution imaging, metallography, Monte-Carlo, nanoparticles, precipitation, transmission electron microscopy
Keywords (user supplied):	electrolytic etching, scanning electron microscopy, phase transformations

PhilMagetchrev190709U

Modeling and kinetic Monte Carlo simulations of the metallographic etching process of second phase particles

Ihor Sobchenko[a+], Dietmar Baither[b], Rudolf Reichelt[a], and Eckhard Nembach[b]*

[a] Institut für Medizinische Physik und Biophysik, Universitätsklinikum, Universität Münster, Robert-Koch-Strasse 31, 48149 Münster, Germany

[b] Institut für Materialphysik, Universität Münster, Wilhelm-Klemm-Strasse 10, 48149 Münster, Germany

[+]Permanent address: Department of Theoretical Physics, Cherkasy National University, Shevchenko Blvd. 81, 18031 Cherkasy, Ukraine

*Corresponding author. E-mail: nembach@uni-muenster.de

Phone: ++49-251-83-33570, Fax: ++49-251-83-38346

Abstract

Kinetic Monte Carlo simulations of the chemical and electrolytic etching processes of nano-scale particles in two-phase materials have been performed. Etching produces a surface relief, which can subsequently be studied by optical, scanning electron, and atomic force microscopy to obtain quantitative information on the size, shape, and spatial arrangement of the particles. The present simulations yield insight into the dependence of the etched relief on the strengths of the atomic bonds in the two phases and on the shape of the particles. Lower limits for the difference in bond energies necessary (i) to reveal the particles and (ii) to avoid over-etching are established. The results of the simulations are discussed with reference to actual etching experiments performed for nano-scale precipitates.

Keywords: Chemical etching; electrolytic etching; metallography; Monte Carlo; nano-particles; precipitates; high-resolution imaging; atomic force microscopy; transmission electron microscopy; scanning electron microscopy; phase transformations.

1. Introduction

The macroscopic physical properties of two- and multiphase materials are governed by two groups of parameters: (a) intrinsic properties of the constituent phases, e.g. crystal structure, electronic band structure, some dislocation parameters, saturation magnetization and (b) geometric parameters: size, shape, and spatial arrangement of the particles of the secondary phases. The latter dependence (b) is most striking in the two following examples [1]:

(i) As the average size of nano-scale coherent ductile particles in particle strengthened materials increases during ageing while the total volume fraction of the particles stays constant, the yield strength first increases with ageing time, then passes through a maximum, and finally decreases. This sequence of states is referred to as the under-, peak-, and over-aged ones, respectively.

(ii) The coercive force of ferromagnetic materials shows a similar dependence on the size of nano-scale coherent non-magnetic particles; there is, however, no over-aged state.

It is standard practice in metallography to derive the quoted geometric parameters of second phase particles from microscopic studies of the surface of the material. Generally some etching procedure is necessary to obtain satisfactory contrast. This holds with few exceptions for optical as well as for atomic force microscopy (AFM) [2-4]; also in scanning electron microscopy (SEM) [3,4] etching is helpful. Three of the few cases for which no etching is needed, are: optical

interference microscopy [5], some rare cases of AFM [2], and magnetic force microscopy of ferromagnetic materials [3]. Chemical and electrolytic etching procedures take advantage of the fact that different phases are dissolved at different rates. Thermal etching works similarly [5]; ion beam etching, however, is more complex because knock-on processes and high-energy-density-zones have to be taken into consideration [6,7]. The surface relief created by etching can subsequently be imaged with satisfactory contrast. For the sake of clarity, up to the end of this section it is assumed that the particles dissolve faster than the matrix. But since the ratio of the dissolution rates of the particles and of the matrix is finite, also the matrix is attacked to some degree. Hence the pits marking the original positions of the etched away parts of the particles will be too large. This is called over-etching, it may cause serious errors in the quantitative characterization of small particles.

In the progress of quantitative AFM and SEM characterizations of nano–scale plate-shaped coherent precipitates of the disordered γ-phase in an $L1_2$-long range ordered γ'-matrix, the need arose to relate the size of the etch-pits left behind by the etched away parts of the γ-precipitates to their actual dimensions [3]. The overall chemical composition of the material was $Ni_{69}Co_9Al_{18}Ti_4$. The main difference in the chemical compositions of the two phases is that the γ-plates are richer in cobalt than the γ'-matrix. The arrangement of the two phases in $Ni_{69}Co_9Al_{18}Ti_4$ is inverse to that in γ'-strengthened nickel-base superalloys, in which the disordered γ-phase forms the matrix and particles of the $L1_2$-long range ordered γ'-phase precipitate [1,2,4,8]. The habit planes of the γ-plates in $Ni_{69}Co_9Al_{18}Ti_4$ are of the type {001}. Preferential etching of the γ-plates occurred as a side effect of the standard preparation procedure of thin foils for transmission electron microscopy (TEM): twin-jet electrolytic polishing [3]. Without any further preparation specific to the applied microscope, the same foils were studied by AFM, SEM, and TEM.

Fig. 1 shows AFM-, SEM-, and TEM-images of such thin foils. The γ-pits left behind by the etched away parts of the plate-shaped γ-precipitates are clearly visible. The nominal indices of the macroscopic surface of the thin foil and hence of the image plane are (001). There are two families of edge-on γ-plates; the indices of their habit planes are (100) and (010). The in-plane γ-plates lie along (001). These micrographs will be discussed in detail in Section 3. In Figs. 1a and b quantitative information on AFM-imaged profiles of γ-pits is given. It is emphasized that measured AFM-profiles are determined by the actual shape of the γ-pits and by the geometry and inclination of the tip of the AFM [3]. The question was what were the actual size and shape of the γ-plates? To solve this problem their size was also determined by TEM of thin foils and computer simulations of the etching

process were undertaken. The TEM study and the simulations proved that the actual size and shape of the γ-precipitates can be accurately derived from AFM-images of the γ-pits.

This former work was the starting point for a more general investigation of the etching processes of two-phase materials: presently three-dimensional kinetic Monte Carlo simulations [9-11] were performed. Both cases were treated: (i) the atomic binding energies in the particle are smaller than those in the matrix, i.e. the particles dissolve faster than the matrix – as in $Ni_{69}Co_9Al_{18}Ti_4$ – and (ii) the opposite case, i.e. the matrix dissolves faster than the particles. The difference in dissolution rates was varied widely. Three different particle shapes were considered. The procedures and the results obtained are reported below. In Section 3.1 these results are compared with those of actually etching γ-precipitates in $Ni_{69}Co_9Al_{18}Ti_4$.

2. Modeling and simulations

The modeled crystal structure, geometries, and etching procedures were as follows. Throughout this communication the etchant will be supposed to be liquid, i.e. chemical and electrolytic etching are simulated. Simulations of thermal etching are quite similar.

2.1. Crystal structures and geometries

The specimen consists of two phases. Both, the particle as well as the matrix, are supposed to have the f. c. c. crystal structure, the same lattice constant a_0, and to be fully coherent. Since in the present model the number of neighboring atoms governs the dissolution rates of the atoms (Section 2.2) and this number depends on the crystal structure, the latter has to be fixed. The simulation procedures described below can easily be adapted to any other crystal structure.

The three most common particle shapes are treated: spheres, plates, and cubes with rounded edges and corners. Incidentally, the γ'-precipitates in advanced commercial γ'-strengthened nickel-base superalloys are examples of such rounded cubes with edge lengths around 500nm [8]. The coordinates of the points on the matrix-particle phase boundary are given by Eq. (1); the center of the particle is at the origin of the coordinate system:

$$\left(\frac{|x|}{\alpha}\right)^n + \left(\frac{|y|}{\alpha}\right)^n + \left(\frac{|z|}{\beta}\right)^k = 1 \quad . \qquad (1)$$

This equation describes a superellipsoid [3,12,13]. The parameters α, β, n, and k determine its shape. Eq. (1) is a unified convenient description of the geometry of all common convex particle shapes: spheres, cubes, plates, fibers. The z-axis has fourfold rotational symmetry and the three planes characterized by $x \equiv 0$, $y \equiv 0$, and $z \equiv 0$ are mirror planes. There are two obvious generalizations of

Eq. (1). The fourfold rotational symmetry of the z-axis can be reduced to a twofold one by replacing the two first terms in Eq. (1) by $\left(|x/\alpha_1|\right)^{n_1}$ and $\left(|y/\alpha_2|\right)^{n_2}$, respectively, with $n_1 \neq n_2$ and / or $\alpha_1 \neq \alpha_2$. Moreover, the mirror symmetry of the plane $z \equiv 0$ can be broken by assigning β and / or k different values in the two half-spaces $z>0$ and $z<0$ [13].

In the present simulations the following values are inserted for α, β, n, and k; they yield the most common shapes of second phase particles:

sphere: $\alpha=\beta=69.5a_0$, $n=k=2$,

plate: $\alpha=69.5a_0$, $\beta=9.5a_0$, $n=k=3$,

cube with rounded edges and corners: $\alpha=\beta=69.5a_0$, $n=k=10$.

Evidently the maximum extensions of all three particles are the same along the [100]– and the [010]–directions. Three–dimensional sketches are shown in Fig. 2. The exponents $n=k=3$ chosen for the plate are those found for the average plate-shaped γ-precipitate in $Ni_{69}Co_9Al_{18}Ti_4$ [3] and the aspect ratio $\alpha/\beta = 7.3$ is close to that of the average γ-precipitate. However, the individual lengths α and β quoted above for the modeled plate amount to only about one eighth of those of the average γ-plate. It is emphasized that the γ-plates in $Ni_{69}Co_9Al_{18}Ti_4$ had neither the shape of flat cylinders, nor of flat cuboids, nor of flat standard ellipsoids, but that they could be very well described as superellipsoids with $n=k=3$ [3]. In the case of plate-shaped particles, etching along one of the two longer axes must be distinguished from etching along the short axis, i.e. the plates may be orientated either normal or parallel to the original {001}-surface of the specimen. Correspondingly two different orientations of the plate-shaped etch-pits must be distinguished: edge-on and in-plane orientation (Fig. 1). The volume V of the superellipsoid is given by

$$V = q_V(n,k) \ \pi \alpha^2 \beta \qquad (2)$$

with $q_V(2,2)=4/3=1.333$ (sphere), $q_V(3,3)=1.813$ (plate), and $q_V(10,10)=2.443$ (rounded cube) [3,13]. The habit plane of the plate and the sides of the rounded cube have the indices {001}.

The particle is embedded in a matrix-cube having {001}-surfaces. Its dimensions are: $350a_0 \times 350a_0 \times 350a_0$. This cube and the spherical particle contain $\approx 172 \times 10^6$ and $\approx 5.6 \times 10^6$ atoms, respectively. Periodic boundary conditions are imposed such that an infinite

(001)-solid-etchant interface is created and etching is along the +z-direction. Only for the simulation of etching along the longer half-axis of the plate [edge-on orientation], this interface has the indices (010) and etching is along the +y-direction. It is tempting to make use of the symmetry of the system and to simulate only one quarter of it. But since this is not fully compatible with the random nature of the dissolution process (Section 3.1.2), it was presently not done. The centre of all particles has the coordinates (0,0,0). With the only exception of the in-plane plate, the matrix-cube is centered at (0, 0, 174.5a_0 - α). In the case of the in-plane plate the centre of the matrix-cube is at (0, 0, 173a_0 - β). Evidently, at the start of the simulations the sphere, the edge-on plate, and the rounded cube are covered by just one atomic layer of matrix; in the case of the in-plane plate there are four such layers.

2.2. Modeling and simulations

The activation energy for transferring an atom from the surface of the particle or from the surface of the matrix to the etchant is E_p and E_m, respectively. These energies are assumed to be proportional to the number ν of first nearest neighbor atoms in the solid phases; hence E_p and E_m are low for atoms at edges and corners:

$$E_p = \nu\ e_p \qquad (3a)$$

and

$$E_m = \nu\ e_m \qquad (3b)\ .$$

Since the coefficients e_p and e_m are related to the energies required for breaking one first nearest neighbor bond in the particle or in the matrix, respectively, for simplicity in the following e_p and e_m will be referred to as first nearest neighbor bond or binding energies. Of course, in the case of metals the term “bond” is not quite appropriate. Effects of more distant neighbors will be discussed in Section 2.4.2. All energies are normalized to k_BT, where k_B is the Boltzmann constant and T the absolute temperature. E_p and E_m are calculated with Eqs. (3) even if some bonds cut through the particle-matrix phase boundary; i.e. Eqs. (3) are applied irrespective of the fact that some of the nearest neighbor atoms may be in the other solid phase. If, however, the fraction of particle atoms which have nearest neighbors in the matrix, is appreciable, bonds crossing the phase boundary must be assigned energies which differ from e_p and e_m. This will be necessary if the extension of the particle in one or more directions is very small; i.e. if the particle is very small or if the plate is very thin. Phases consisting out of more than one type of atoms are referred to in Section 2.4; for such materials e_p and e_m in Eqs. (3) may be considered as suitable averages.

The number ν of the present (001)- and (010)-solid-etchant interfaces of the three dimensional f. c. c. crystal ranges from four for an add-on atom to eight for an atom in a perfect

{001}-interface, whereas ν of a two dimensional simple square lattice varies only between one and three. Evidently, realistic results can only be derived from simulations of three-dimensional crystals.

The range of e_p and e_m covered in the present kinetic Monte Carlo simulations is 1.0-3.4 and the ratio e_m/e_p is between 1/1.3 and 1.3. This range of e_p and e_m is close to the one covered by Strobel et al. [14] in their kinetic Monte Carlo simulations of Ostwald ripening. Moreover the present highest value 3.4 is close to one half of the actual, normalized (to k_BT, T=300K) bulk first nearest neighbor pair-interaction energies $\varepsilon_{Cu\,1}$ and $\varepsilon_{Ni\,1}$ of copper and nickel, respectively. In Table 1 the values of $\varepsilon_{Cu\,j}$ and $\varepsilon_{Ni\,j}$, $1 \le j \le 3$, of the first three coordination shells are listed. $\varepsilon_{Cu\,j}$ and $\varepsilon_{Ni\,j}$ were derived from the pair potential functions published by Mishin et al. [15,16] by inserting the respective shell radii r_j. The quoted authors have shown that lattice properties calculated on the basis of their pair potential functions agree well with experimental data.

Since only the N atoms at the surface of the solid can be dissolved, only they are considered. At the start of the kinetic Monte Carlo simulation the solid-etchant interface is a perfect (001)-plane [(010)-plane for the edge-on plate] with $N \approx 0.25 \times 10^6$ atoms. As stated above, etching is along the $+z$-direction [along the $+y$-direction for the edge-on plate]. The simulation of the dissolution of one atom will be referred to as one step; each step involves three sub-steps:

(i) With the aid of Eqs. (3) the relative, non-normalized thermodynamic probability p_i of the dissolution of atom No. i is calculated. This is done for all N interface atoms. Eqs. (4a) and (4b) hold for particle and matrix atoms, respectively:

$$p_i = e^{-E_{p,i}} \qquad (4a)$$

and

$$p_i = e^{-E_{m,i}} \quad , \qquad (4b)$$

$1 \le i \le N$. The pre-exponential factors of both phases are assumed to be the same; hence these factors are disregarded.

(ii) The ratio s_μ, $1 \le \mu \le N$, is calculated

$$s_\mu = \sum_{j=1}^{\mu} p_j \Big/ \sum_{j=1}^{N} p_j \quad . \qquad (5)$$

s_0 is zero and s_N equals unity.

(iii) A uniform random number w, $0 \le w \le 1$, is generated and the atom No. n, $1 \le n \le N$, for

which $s_{n-1} < w \leq s_n$ holds, is transferred from the solid to the etchant.

Evidently the probability that atom No. n is dissolved in this step equals $p_n / \sum_{j=1}^{N} p_j$. Subsequently the next step is started for the new solid-etchant interface, which differs from the previous one, because one atom has been removed in the previous step. Exactly one atom is dissolved in each step. The total number of steps required to entirely dissolve the particle depends on its shape and on e_p and e_m. This will be demonstrated in the figures presented in the following section.

2.3. Results of the kinetic Monte Carlo simulations

A choice of simulation results is presented in Figs. 3-8. Throughout the following the term "front of etching" refers to the most advanced point of the solid-etchant interface. If e_p is smaller than e_m, the particle dissolves faster than the matrix and vice versa. In the latter case, $e_p > e_m$, during intermediate stages of etching the particle protects the matrix lying directly under it from the attack by the etchant (Figs. 3, 5, 6h), but finally the particle becomes completely detached from the matrix. In Figs. 3-5 dark grey lines outline the periphery of such free particles. Animations of simulated etching processes are available for all presently studied particle shapes and for two combinations of normalized binding energies: e_p=1.70, e_m=2.21 and e_p=2.21, e_m=1.70 [17]. The effects of varying the ratio e_m/e_p of the normalized binding energies, while keeping e_m constant, are demonstrated in Fig. 7 for the spherical particle. Since Eqs. (4) are non-linear the etched profile does not only depend on the ratio e_m/e_p, but also on the individual values e_p and e_m; this is shown in Fig. 8 for $e_m/e_p \equiv 1.15$. Fig. 8 demonstrates what happens if the temperature T is varied while the non-normalized (to $k_B T$) activation energies for dissolution are kept constant: T decreases from Fig. 8a to 8f. From Figs. 3-8 the following results are extracted. Though not all of them can be proved within reasonable times for all combinations of e_p and e_m in the entire range $1.0 \leq e_p, e_m \leq 3.4$ presently studied, all listed results are considered as reliable. This is emphasized for results Nos. A2) and A3). Results Nos. A1), A5), B1), B2.1), B2.2), and B2.4) are direct consequences of Eqs. (3), according to which the activation energy for the dissolution of an atom is proportional to the number ν of its first nearest neighbors: ν of atoms at edges and corners is relatively low and high in the most densely packed {111}-planes.

Results:

A) General

A1) The roughness of the solid-etchant interface is low: plus / minus 1-2 atomic diameters (see B2.1) below). This can be inferred from Fig. 6 and from the animations [17]. Moreover it is indicated by the small wiggles of the curves representing the interface in Figs. 3-5, 7, and 8.

A2) Over-etching is quite frequently observed: if the particle dissolves faster than the matrix, the resulting etch-pit is too large and in the opposite case the remainder of the particle, which sticks out of the matrix, is too small. In intermediate stages of etching the solid-etchant interface stays the closer to the original matrix-particle phase boundary the larger the term $\left|e_p - e_m\right|$ is (see also B2.3) below). If the ratio e_m/e_p is smaller than 1/1.3 or larger than 1.3 and etching does not continue too long, over-etching is almost negligible (Figs. 3-5) for all particle shapes and orientations presently considered. If after etching the largest extension of the original particle is not close to the surface of the specimen, the size of the particle may be underestimated (Figs. 3 and 4).

A3) Even if e_p and e_m differ by as little as 5%, etching reveals a spherical particle (Figs. 7c, d). Though no simulations have been performed to establish analogous limits for the other particle shapes, it is expected that similar limits apply also for them.

A4) Due to the non-linearity of Eqs. (4) the etched profiles do not only depend on the ratio e_m/e_p but also on the individual values of e_p and e_m. This dependence is strongest if both bond energies are rather low (Fig. 8).

A5) Far away from the particle, respectively from the etch-pit, the matrix is planar - except for steps of atomic height - and follows (001)-planes [(010)-planes for the edge-on plate]; this proves that the matrix-cube is sufficiently large.

B) The particle dissolves faster than the matrix: $e_p < e_m$

B1) At the very beginning of etching several small shallow pits appear. Later they coalesce and a single deep pit is formed at the original site of the particle (e.g. Figs. 5a and b, animation [17], and Section 3.1.2). This primarily concerns the rounded cube and the in-plane plate, which have an almost flat, respectively a rather flat top interface with the etchant.

B2) After an appreciable amount of the particle has dissolved, several different types of particle-etchant interfaces can be distinguished:

B2.1) Much of the interface is along terraces of the most densely packed {111}-planes. This can be seen best in Figs. 3 and 6 and in the animations [17]. In Figs. 3a and b showing the sphere, the traces of the solid-etchant interface are along the [101]-direction, which lies in the intersection of the $(\bar{1}11)$-plane with the $(\bar{1}\bar{1}1)$-plane, and along the $[\bar{1}01]$-direction, which lies in the intersection of the (111)-plane with the $(\bar{1}1\bar{1})$-plane. In the pseudo-three-dimensional presentation of the cubic particle shown in Fig. 6c two families of {111}-planes are visible;

the other two families of {111}-planes are in the cut away front half of the matrix-cube. The height of the steps between adjacent {111}-terraces is of atomic dimensions. At constant ratio e_m/e_p the predominance of {111}-planes is most pronounced if the normalized binding energies e_m and e_p are high, i.e. the temperature is low (Fig. 8). The reason for this energy dependence is the non-linearity of Eqs. (4).

B2.2) The central area of the bottom solid-etchant interface of a partially dissolved cubic particle is along (001)-planes (e.g. Figs. 3e, f and 6c).

B2.3) When the solid-etchant interface reaches the particle-matrix phase boundary, etching slows down drastically because from then on it is governed by e_m, which is higher than e_p. Hence this interface stays close to the original phase boundary, see e.g. the upper part of the spherical particle in Fig. 3a and the sides of the rounded cube in Fig. 3e.

B2.4) After the entire spherical particle and an appreciable amount of the matrix below the original position of the particle have been dissolved, much of the surface of the etch-pit is formed by {111}-and {001}-planes (Fig. 3). A pit remains discernable for very long etching times.

C) The matrix dissolves faster than the particle: $e_p > e_m$

C1) The most conspicuous effect has already been mentioned: at intermediate stages of etching the particle protects the matrix lying directly under it from the attack by the etchant, but later the particle completely loses contact to the matrix (Figs. 3, 5, 6h). As to be expected it is the in-plane plate which becomes detached from the matrix at the lowest total number of dissolved atoms. After a particle has become free, during further etching all traces of it in the surface of the matrix disappear very soon.

C2) Etching exposes different families of crystallographic planes of the spherical particle. This is easily noticeable for e_m=1.92 and e_p=2.21 in Fig. 3d. If the difference between e_p and e_m is larger, e.g. e_m=1.70 and e_p=2.21 in Fig. 3c, the sphere becomes completely free before it changes its shape markedly. The analogous effects for the rounded cube are less pronounced because planes close to {001} persist for long times of etching (Figs. 3g, h).

C3) For $e_p > e_m$, the front of etching proceeds much more slowly than for $e_p < e_m$ (see B) above) because most of the top area of the matrix is rather flat and much more atoms must be dissolved before the same maximum depth is reached (Figs. 3-5).

2.4. Secondary effects

There are several processes which may affect etching beyond that which has been considered so far. Seven of them are listed here and the two first ones will be analyzed in the subsequent sections:

(i) After a particle which dissolves faster than the matrix, has been etched very deeply it becomes difficult to provide fresh etchant at the bottom of the pit and to remove the dissolved atoms from it. The ensuing effects will be analyzed in Section 2.4.1.

(ii) The possible effects of second and third nearest neighbor bonds have already been referred to and will be discussed in Section 2.4.2.

(iii) The number ν of first nearest neighbor atoms depends on the crystallographic orientation of the solid-etchant interface, e.g. ν equals eight for the perfect {001}- and nine for the perfect {111}-interface (Table 1). Hence the etching process may vary with the orientation of the original interface.

(iv) The binding energies e_p and e_m may vary with ν. This can be modeled by adding higher order terms of ν on the right hand sides of Eqs. (3).

(v) In Section 2.2 it has already been mentioned that in the case of very small particles and very thin plates it will be appropriate to allow for the fact that bonds which cut through the particle-matrix phase boundary have energies which differ from e_p and e_m.

(vi) If a particle which dissolves faster than the matrix, is surrounded by a strain field, over-etching is likely to occur. This can be simulated by lowering e_m in the region of the strain field.

(vii) In general the matrix as well as the particle will consist out of more than one type of atoms. This can be allowed for when the crystal is built up in the computer. In such cases e_p and e_m depend on the types of neighboring atoms. This point is of importance for long range ordered phases; for them the present normalized energies e_p and e_m may be considered as averages.

2.4.1. Effects of a lack of fresh etchant in the etch-pit

If the etch-pit left behind by the etched away parts of a particle which dissolves faster than the matrix, is narrow and deep it becomes difficult to provide fresh etchant at the bottom of the pit and to remove the dissolved atoms from it. The relevant processes are governed by a host of parameters: e.g. shape and size of the pit, convection and diffusion of the etching agent and of the dissolved atoms, viscosity of the etchant, its adhesion to the solid. As mentioned, the ensuing effects become serious if the pit is deep and narrow or has a bottle neck at its top. Such a neck is formed e.g. if the particle has the shape of a sphere and the binding energy e_p is appreciably smaller than e_m (Figs. 3a and 6a). Instead of attempting to take all relevant processes into consideration just the two basic features of the hindrances to the etching process are allowed for in the present kinetic Monte Carlo simulations for a spherical particle: the narrower the upper part of the pit is and the deeper it is, the more significant are these hindrances.

The mathematical formulation for etching along the z-direction is as follows. The coordinates of all atoms are integer multiples of ½a_0, where a_0 is the lattice constant. To calculate the non-normalized probability p_1 (Eqs. (4)) of dissolving the atom (particle or matrix atom) having the coordinates (x_1, y_1, z_1), the right hand sides of Eqs. (4) are multiplied by the function $\Phi(z_1)$, which is related to the probability that the etchant agent penetrates to the depth z_1:

$$\Phi(z_1) = \exp\{ -\lambda (z_1 - z_m)^2 / A \} \qquad \text{for} \quad (z_1 - z_m) > a_0 \tag{6}$$

and $$\Phi(z_1) = 1.0 \qquad \text{for} \quad (z_1 - z_m) \le a_0 \quad ,$$

where λ is a numerical coefficient, z_m the average z-level of the matrix far away from the pit where the matrix is planar, and A is an average over the area of all cross-sections of the pit with $z_m \le z \le z_1$:

$$A = \frac{\sum_{j=2z_m/a_0}^{2z_1/a_0} S_j^*}{2(z_1 - z_m) / a_0} \quad . \tag{7}$$

To allow for a bottle neck of the pit, not the actual cross-section at the level $z = ja_0/2$ is inserted into the sum, but S_j^*, which is the minimum area of all cross-sections with $z_m \le z \le ja_0/2$. If the pit narrows continuously as z increases, A is the arithmetic mean cross-section. The limitations $(z_1 - z_m) > a_0$ and $(z_1 - z_m) \le a_0$ in Eq. (6) have two consequences: (i) $\Phi(z_1)$ is not affected by the roughness of the solid-etchant interface (Section 2.3) and (ii) $\Phi(z_1)$ is smaller than unity only if the respective atom lies in the surface of the etch-pit. Two alternative values are inserted for the coefficient λ: 0.2 and 1.0. For $\lambda = 0$, the standard results presented in Section 2.3 and Fig. 3 are recovered. Evidently the effects of a lack of fresh etchant are the more serious the larger the extension of the the particle along the z-direction is. The results for the spherical particle and e_p=1.70 and e_m=2.21 are shown in Fig. 9. As the ratio $\{ (z_1 - z_m)^2 / A \}$ increases, $\Phi(z_1)$ becomes small and the advancement of the front of etching slows down. This effect is the stronger the larger λ is. A comparison of Fig. 3a with Fig. 9 leads to the following conclusions:

(1) Due to the term $(z_1 - z_m)^2$ in Eq. (6), for $\lambda > 0$ the (001)–bottom of the etch-pit is flat and wide. This effect is enhanced by small areas A.

(2) At a given position of the front of etching in the particle, i.e. at given value of δ in Figs. 3a and 9, the number of dissolved atoms increases drastically with λ.

(3) The larger λ is, the more matrix atoms next to the original particle-matrix phase boundary dissolve before the front of etching reaches the bottom of the particle. As to be expected this enhances over-etching.

2.4.2. Effects of interactions with second and third nearest neighbor atoms

So far only the interactions with first nearest neighbor atoms have been taken into consideration in the kinetic Monte Carlo simulations. In this section the effects of second and third nearest neighbor interactions are analyzed. Besides the normalized first nearest neighbor bond energies e_p and e_m, the respective second nearest neighbor energies e_p^* and e_m^* and the third nearest neighbor energies e_p^{**} and e_m^{**} are allowed for. Eqs. (3a) and (3b) for the activation energies E_p and E_m for dissolution are replaced by Eqs. (8a) and (8b), respectively:

$$E_p = \nu\, e_p + \nu^* e_p^* + \nu^{**} e_p^{**} \qquad (8a)$$

and

$$E_m = \nu\, e_m + \nu^* e_m^* + \nu^{**} e_m^{**} \quad , \qquad (8b)$$

where ν, ν^*, and ν^{**} are the numbers of first, second, and third nearest neighbor atoms, respectively. Introducing the ratios $e_p / e_p^* = \rho_{p1}$, $e_m / e_m^* = \rho_{m1}$, $e_p / e_p^{**} = \rho_{p2}$, and $e_m / e_m^{**} = \rho_{m2}$ into Eqs. 8(a) and 8(b) yields

$$E_p = e_p (\nu + \nu^* / \rho_{p1} + \nu^{**} / \rho_{p2}) \qquad (8c)$$

and

$$E_m = e_m (\nu + \nu^* / \rho_{m1} + \nu^{**} / \rho_{m2}) \quad . \qquad (8d)$$

For the sake of argument the ratios ρ_{p1}, ρ_{m1}, ρ_{p2}, and ρ_{m2} are related to the normalized pair interaction energies $\varepsilon_{Cu\,j}$, $1 \le j \le 3$, of copper introduced in Section 2.2 and listed in Table 1: $\rho_{p1} = \rho_{m1} = \varepsilon_{Cu\,1} / \varepsilon_{Cu\,2} = 3.36$ and $\rho_{p2} = \rho_{m2} = \varepsilon_{Cu\,1} / \varepsilon_{Cu\,3} = 24.9$. Evidently, allowing for the interactions with second and third nearest neighbors is equivalent to raising the effective number of first nearest neighbors. The additional terms may seem small. p_i, which governs the probability of dissolving an atom (Eqs. (3) and (4)), is, however, lowered by the factors $\exp[- e_p (\nu^* / 3.36 + \nu^{**} / 24.9)]$ and $\exp[- e_m (\nu^* / 3.36 + \nu^{**} / 24.9)]$, respectively. For a perfect {001}-plane and e_p=1.70, this factor amounts to 1/28.5 and for e_m=2.21 it is 1/77.8 . Allowing for second and third nearest neighbor interactions has the effect of amplifying the difference in the dissolution probabilities brought about by the first nearest neighbor interactions.

Moreover, v^* and v^{**} tend to increase with v: an atom located at an edge or corner has relatively few first nearest neighbors as well as relatively few more distant ones.

Interactions with more distant neighbors affect {111}- and {001}-planes to different degrees. Let $E(\mu, hkl)$ be the activation energy for the dissolution of an atom in a perfect $\{hkl\}$-plane and μ is the number of coordination shells allowed for. The ratios $E(1,111)/E(1,001)$, $E(2,111)/E(2,001)$, and $E(3,111)/E(3,001)$ equal 1.13, 1.04, and 1.05, respectively. They decrease as μ increases, but not monotonically. This non-monotonic variation of these ratios with μ is not caused by the present choice of ρ_{pi} and ρ_{mi}, but by the dependence of v^* and v^{**} on the indices $\{hkl\}$. $E(1,111)/E(1,001) > E(3,111)/E(3,001) > E(2,111)/E(2,001)$ holds for $1.75\rho_2 > \rho_1 > 0$.

Some results of the simulations for a spherical particle with e_p=1.92 and e_m=2.21 are presented in Fig. 10. There both cases are shown: allowing (i) for first and second and (ii) for first, second, and third nearest neighbor bonds. These simulations are very time consuming. The most important result is that unless the particle has been completely dissolved, the width of the top of the etch-pit is nearly independent of the number μ, i.e. over-etching is independent of μ. Again {111}- and {001}-planes are exposed. The interactions with more distant neighbor atoms flatten the (001)-bottom of the etch-pit in the particle; this effect is similar to that of a lack of fresh etchant at the bottom of the etch-pit (Fig. 9, Section 2.4.1). The width of the (001)-bottom does not increase monotonically with μ: the bottom is widest for $\mu = 2$. This is tentatively interpreted to be due to the above stated variation of the ratios of the {111}- and {001}-activation energies with μ: as μ is raised, they approach each other, but not monotonically. Low ratios $E(\mu,111)/E(\mu,001)$ favor the exposure (not the dissolution rate!) of {001}-planes and thus widen the (001)-bottom of the etch-pit. As long as the particle has not completely dissolved, the numbers ω_2 and ω_3 of dissolved atoms (Fig. 10) are smaller than ω_1. There are two mechanisms which contribute to this effect: (i) the amplification of differences in dissolution rates for μ>1 mentioned above in connection with Eqs. (8) and (ii) the variation of the ratio $E(\mu,111)/E(\mu,001)$ with μ, due to which the dissolution rate of atoms in the (001)-matrix-surface is less favored for μ>1 than for μ=1. Hence relative fewer atoms of this (001)-matrix-surface are dissolved for μ>1. Since its area is large, this effect outweighs that of widening the etch-pit.

3. Discussion: Comparison of Monte Carlo Simulation with TEM Results

Most of the results of the kinetic Monte Carlo simulations of etching have already been discussed in Sections 2.3 and 2.4. However, it remains to relate them to the etching experiments carried out for the plate-shaped precipitates of the γ-phase in $Ni_{69}Co_9Al_{18}Ti_4$ [3] (Section 1). AFM-, SEM-, and TEM-images of them are presented in Fig. 1. Since the γ-plates dissolve faster than the γ'-matrix, etching produces γ-pits. Hence in Sections 3.1 and 3.2 only the case $e_m > e_p$ is considered. The three types of microscopes yield complementary information; quantitative data on the depth profile of the γ-pits are most easily obtained by AFM. If the slope of the surface relief of the specimen changes abruptly, the geometry and the inclination of the tip of the AFM must be taken into consideration [3] (Section 1). It turned out to be very difficult to unambiguously determine the real shape of the plate-like γ-precipitates in $Ni_{69}Co_9Al_{18}Ti_4$ by using the experimental data of only one of the three applied microscopic methods [3]. If, however, the data obtained by one microscope are complemented by computer simulations of the etching process, the reliable characterization of the γ-precipitates is possible. In Sections 3.1.2 and 3.2 the actual shapes of the γ-precipitates and of the γ-pits will be derived from the micrographs and subsequently these shapes will be discussed with reference to the respective relieves obtained in the simulations. The original surface of the specimen is parallel to (001).

3.1 In-plane γ-plates

The AFM-, SEM-, and TEM-images of in-plane γ-pits in $Ni_{69}Co_9Al_{18}Ti_4$ shown in Fig. 1 deviate somewhat from perfect four-fold rotational symmetry. There are two groups of entirely different effects which may give rise to asymmetries: (i) the two longer axes of the γ-plates themselves may differ in length and (ii) etching may produce asymmetric γ-pits even if the γ-plates are perfectly symmetric. These two groups are discussed in the following.

3.1.1 Asymmetry of the γ-plates

The growth rate of each γ-plate in $Ni_{69}Co_9Al_{18}Ti_4$ is governed by the surrounding concentration gradients of the precipitating elements. These gradients are affected by neighboring γ-plates, the nucleation of which occurs at random. Hence the growth rate of in-plane γ-plates may be different along the [100]- and along the [010]-direction. The average difference in length of the two longer half-axes of the in-plane γ-plates was experimentally found to be ±10% [3].

3.1.2 Asymmetric etching

Since the aspect ratio α / β (=longer axis / shorter axis) of the majority of the γ-plates in $Ni_{69}Co_9Al_{18}Ti_4$ exceeds 7.0 [3], even minor deviations of the actual orientation of the surface of the macroscopic specimen from the exact nominal (001) one have strong effects on the appearance of in-plane γ-pits. The γ-pit marked **B** in Fig. 1a is an example. For a cuboidal pit with the aspect ratio α / β =7.0, a deviation as small as 8.1° from the nominal orientation leads to a depth error $\Delta t = \alpha \, \mathrm{tg} 8.1° = \beta$. The inclination of the bottom of the γ-pit marked **B** in Fig. 1a amounts to about 3.3°; this angle was calculated from the depth profile shown in the upper right of Fig. 1a. It is for such a misorientation that the right corner of **B** is missing. Due to an inclination of the γ-pit relative to the macroscopic surface of the specimen, in the SEM the yields of secondary electrons from opposite - ascending and descending - slopes of the in-plane γ-pit are different. Hence the two slopes appear at different brightness in the micrographs: the upper rims of the γ-pits in Figs. 1c and d are much brighter than the lower ones. There are at least three reasons for deviations of the orientation of the macroscopic surface from (001): (i) errors in cutting the slice from which the thin TEM-foil is prepared, (ii) small angle boundaries in the foil, and (iii) after its electro-polish, its surface is slightly concave. Since the γ-plate is slightly convex (Fig. 2), in a perfectly well orientated specimen the first contact of the etchant with the in-plane γ-plate is most likely to occur at its apex. Hence the dissolution of the γ-plate proceeds from its center towards its corners.

The contrast of secondary electron images primarily depends on the orientation of the surface of the specimen relative to the incident electron beam. Therefore the ascents and descends of in-plane γ-pits yield strong contrast in the SEM. The AFM shows the topography of the specimen, i.e. the contrast is governed by differences in height. In the TEM, however, two entirely different mechanisms strongly contribute to the contrast: strain contrast and thickness contrast [3]. Since the average atomic numbers of both phases in $Ni_{69}Co_9Al_{18}Ti_4$ are nearly the same, there is hardly any atomic number contrast. Strain contrast renders the not yet dissolved parts of partially dissolved in-plane γ-plates visible. Even if an in-plane γ-plate is completely embedded in the γ'-matrix and has no contact with either surface of the foil, the γ-plate may produce strain contrast. At γ-pits the local thickness of the TEM-foil is reduced and thickness contrast is generated.

The white arrows in the SEM-images presented in Figs. 1c and d point at missing corners of the in-plane γ-pits; there their outline is parallel to <011>- instead of to <001>-directions. The reason for these missing corners is that the in-plane γ-precipitates have been dissolved only partially; actually in the apparently missing corners some γ-pockets are still left. Due to their strain contrast they are visible in the TEM. In the AFM and SEM, however, such corners remain invisible. The top

of the pockets may still be covered by γ'-matrix. Facing the bottom of the γ-pits the γ-pockets are delimited by {111}-planes, which may be interrupted by some (001)-terraces [3]. In the TEM these inclined {111}-surfaces yield thickness contour lines along <011>-directions. This is demonstrated in the bright field TEM images shown in Figs. 1e and f. By printing them with inverted contrast, the appearance of the γ-plates becomes similar to that in the other micrographs. The bright thickness contour lines of γ-pit C in Fig. 1e and of that in Fig. 1f are in line with the dotted white lines. The dark square with <011>-boundaries in Fig. 1f is the image of the bottom of the γ-pit; there is thickness contrast. The bottom of C in Fig. 1e is rather asymmetric. The wider bright contrast surrounding the dark bottoms is due to (i) thickness contours and (ii) strain contrast (short white arrows) produced by not yet dissolved γ-pockets. This latter contrast has outer <001>-boundaries. This discussion of the micrographs is summarized as follows: the dissolution of in-plane γ-plates starts near their centers and proceeds towards their corners, which are dissolved last. This is evident in Figs. 1a, c-f. It is for this reason that in AFM- and SEM-images many corners of in-plane γ-pits are missing. Only the TEM reveals these γ-corners because the not yet dissolved γ-pockets produce strain contrast.

The described experimental findings are now discussed with reference to the results of the simulations of the etching process. In Figs. 11a-i, a sequence of nine stages of the simulated development of an in-plane pit is shown. The parameters of the simulation are the same as those in Figs. 5a and 6g: e_p=1.70 and e_m=2.21, i.e. the plate dissolves faster than the matrix. At the beginning, dissolution of the matrix-layers covering the plate starts at several different spots (Figs. 11a, b). Etching reaches the bottom of the plate first directly below its center (Fig. 11d). The reasons for this are: (i) because of the slight upward curvature of the plate (Fig. 2) the matrix-layer covering it is thinnest above the center and the etchant contacts the plate there first and (ii) because e_p is smaller than e_m further dissolution progresses fastest in this region. The random nature of the dissolution process gives rise to asymmetries of the pit, especially at the beginning of the etching process. Though later these asymmetries become weaker they still tend to reduce the local number of nearest neighbor bonds and thus to raise the dissolution rate locally. This explains the bizarre shapes of the simulated in-plane pits at intermediate stages of etching (Figs. 11b-e). Still later (Figs. 11f-h) the interface between the etchant and the remainders of the plate is of the type {111}. The intersections of these {111}-planes with the bottom of the pit are not perfectly straight because (i) the bottom is slightly concave (Fig. 2) and (ii) the {111}-planes are terraced. These results of the simulations agree very well with the experimental results communicated above. The actual TEM-images presented in Figs. 11j-l are very similar to the simulated images in Figs. 11d, f, and h, respectively.

3.2 Edge-on γ-plates

The comparison of micrographs of *edge-on* γ-pits in $Ni_{69}Co_9Al_{18}Ti_4$ with simulated pits is straight forward because the high aspect ratio $\alpha / \beta \approx 7$ of the γ-plates is in favor of *edge-on* γ-plates: minor deviations of the orientation of the macroscopic surface of the specimen from the nominal (001) one are not of any significance. This contrasts with the *in-plane* plates discussed in the preceding section. All micrographs presented in Figs. 1a-e and the depth profile in Fig. 1b show that not only the γ-plates are attacked by the electrolyte but that next to them also the γ'-matrix dissolves to some extent. Hence the rims at the top of the edge-on γ-pits are blunted; evidently there is over-etching. In Ref. [3] it was concluded that there the slope of the γ'-matrix is parallel to {011}-planes, but after very strong dissolution it is parallel to {111}-planes. Moreover, after prolonged etching zigzag shapes of the rims of the edge-on γ-pits were found in the experiments. This was interpreted to have been brought about by a combination of two different families of {111}-planes [3]. Blunting renders the experimental determination of the shorter axis β less accurate than that of the longer axis α. This case of over-etching demonstrates that one has to carefully evaluate the etching process.

The simulations for the edge-on γ-plate have shown that blunting becomes the more serious the smaller the difference (e_m-e_p) of normalized binding energies is (Figs. 4e, f, Section 2.3). In addition there may be effects of a lack of fresh etchant at the bottom of the γ-pit (Section 2.4.1). A close inspection of Fig. 4f revealed that a narrow strip of the shoulders is parallel to (011)-, respectively to $(0\bar{1}\bar{1})$-planes. As long as the particle has not dissolved completely, inside of the pit the solid-etchant interface follows {111}-planes or is close to the original phase boundary (Fig. 6e). As described in Section 2.3, the straight lines along <011> in Figs. 4a and b are in fact traces of {111}-planes. After very long etching, when the particle has dissolved completely, {111}- and (001)-planes are exposed also in the matrix (Figs. 4a, b, e, f, animation [17]). So far the results of the simulations agree very well with the experimental ones [3]. However, no zigzag {111}-slopes of the rims of the edge-on pits were found in the simulations. This contrasts with the experimental results. The reason is probably that the simulated plates were smaller than the actual γ-plates in $Ni_{69}Co_9Al_{18}Ti_4$ by about the factor eight (Section 2.1). If the plates are large, the solid-etchant interface may alternate between two different families of {111}-planes. This alternation may be induced e.g. by local fluctuations of the composition of the solid. There is another process which may lead to zigzag {111}-blunting of the rims of large edge-on γ-pits: in different parts along a rim {111}-blunting may nucleate on two different families of {111}-planes. On the basis of this discussion, it is concluded that the

combination e_p=1.92 and e_m=2.21 of normalized binding energies represents those of the γ-plates and of the γ'-matrix in $Ni_{69}Co_9Al_{18}Ti_4$ quite well. Since the ratio e_m/e_p=2.21/1.92=1.15 is inside the range 1/1.3-1.3, there is some over-etching (Fig. 4f, Section 2.3).

4. Conclusions

Kinetic Monte Carlo simulations of the metallographic etching processes of second phase particles have been performed for their most common shapes: spheres, rounded cubes, and plates. The activation energies for the dissolution of the particles and of the matrix are assumed to be governed by the number and strength of bonds between neighboring atoms. Interactions with up to three shells of neighbors are considered. This model proved to be highly successful. Some of the results are listed here:

1) Provided the nearest neighbor atomic bond energies of the two phases differ by more than about 30%, over-etching is almost negligible for all particle shapes presently studied. Even if these energies differ by only 5% the particles can be revealed by etching. Though this latter 5%-limit has been proven only for the spherical particle, similar limits are likely to hold for the other particle shapes.
2) As to be expected etching exposes densely packed planes. The roughness of the etched specimen surface is very low: plus / minus 1-2 atomic diameters.
3) The results of the simulations obtained for plate-like particles agree very well with experimental AFM, SEM, and TEM results. Simulations are of great help in interpreting AFM-, SEM-, and TEM-images of the plate-like precipitates of the γ-phase in $Ni_{69}Co_9Al_{18}Ti_4$.
4) The simulation procedures can easily be extended to allow for various secondary effects, e.g. (i) those caused by a lack of fresh etchant at the bottom of a deep and narrow etch-pit or (ii) those due to bonds with second and third nearest neighbor atoms. These two secondary effects do not alter the results of the simulations seriously.

Acknowledgements

The authors are highly indebted to Drs. S. Divinskiy, Münster, and D. Rönnpagel, Templin, for discussions, to Dr. J. Pesicka, Prague, for taking the TEM images, and to Prof. Dr. L. Chi, Münster, for making her AFM available to them. Financial support by the Deutsche Forschungsgemeinschaft under the contract No. RE 782/12-1 is gratefully acknowledged.

REFERENCES

[1] E. Nembach. *Particle strengthening of metals and alloys*. (Wiley, New York, 1997).

[2] J. Wosik, H.J. Penkalla, K. Szot, B. Dubiel, F. Schubert, A. Czyrska-Filemonowicz, Prakt. Metallogr. **39** 140 (2002).

[3] I. Sobchenko, J. Pesicka, D. Baither, W. Stracke, T. Pretorius, V. Mohles, L. Chi, R. Reichelt, E. Nembach, Phil. Mag. **87** 2427 (2007).

[4] V.S.K.G. Kelekanjeri, R.A. Gerhardt, Acta Mater. **57** 616 (2009).

[5] R. Telle, G. Petzow. In: R.W. Cahn, P. Haasen, E.J. Kramer, editors. *Materials science and technology*, vol 2A, part I. (VCH Verlagsgesellschaft, Weinheim, 1992) p. 358.

[6] W. Eckstein. *Computer simulation of ion-solid interaction*. (Springer-Verlag, Berlin, 1991).

[7] H.M. Urbassek, Nucl. Instr. Methods Phys. Research B **122** 427 (1997).

[8] E.W. Ross, C.T. Sims . In: C.T. Sims, N.S. Stoloff, W.C. Hagel, editors. *Superalloys II*. (Wiley, New York, 1987) p. 97.

[9] W.M. Young, E.W. Elcock, Proc. Phys. Soc. **89** 735 (1966).

[10] A. Chatterjee, D.G. Vlachos, J. Computer-Aided Mater. Des. **14** 253 (2007).

[11] http://en.wikipedia.org/wiki/Kinetic_Monte_Carlo.

[12] E.W. Weisstein. *Superellipsoid* (MathWorld –A Wolfram Web Resource, 2005); http://mathworld.wolfram.com/Superellisoid.html.

[13] I. Sobchenko, J. Pesicka, D. Baither, R. Reichelt, E. Nembach, Appl. Phys. Letters **89** 133107 (2006).

[14] M. Strobel, K.H. Heinig, W. Möller, Phys. Rev. B **64** 245422 (2001).

[15] Y. Mishin, D. Farkas, M.J. Mehl, D.A. Papaconstantopoulos, Phys. Rev. B **59** 3393 (1999).

[16] Y. Mishin, M.J. Mehl, D.A. Papaconstantopoulos, A.F. Voter, J.D. Kress, Phys. Rev. B **63** 224106 (2001).

[17] Animations of kinematic Monte Carlo simulations of etching processes; http://www.uni-muenster.de/Physik.MP/Simulieren/.

FIGURE CAPTIONS

Fig. 1: (a, b) Raw data AFM topographs of plate-shaped γ-precipitates (actually of the γ-pits left behind by the etched away parts of the γ-precipitates) in $Ni_{69}Co_9Al_{18}Ti_4$. **A** marks the same edge-on γ-pit in (a) and (b) and **B** an in-plane one in (a). At the top right, AFM-line scans of the depth profiles between the two points marked by circles and by the numbers 1 and 2 are shown. The length of the black vertical double arrows corresponds to 100nm depth; the depth scale is the same as that in the *x*-*y*-plane. (b) Depth relief of the edge-on γ-pit **A**; the difference in depth between neighboring contour lines is 15nm. (c, d) Secondary electron SEM- and (e, f) bright field TEM-images printed as negatives. The short white arrows in (c-f) and the dotted white lines in (e, f) are explained in Section 3.1.

Fig. 2: Sketches of superellipsoids: sphere, plate, rounded cube. The parameters α, β, n, and k govern the shape of the superellipsoid (Eq. (1)).

Fig. 3: Successive stages of the simulated etching process of a spherical (left) and a cubic (right) particle; the original particle shape is shaded. The curves indicate the solid-etchant interface. The image plane is the plane $y \equiv 0$, i.e. a cross-section through the center of the particle is shown. The whole vertical extensions of both particles amounts to $139a_0$. The total range of the abscissa (from $-175a_0$ to $+175a_0$) equals the full extension ($350a_0$) of the matrix cube. The normalized binding energies e_p and e_m are indicated. δ is the approximate (± 1) z-coordinate (in units of a_0) of the front of etching (=most advanced point of the solid-etchant interface) and ω is the respective approximate number (in units of 10^6) of steps performed (=number of dissolved atoms). (a, b, e, f), $e_p<e_m$; (c, d, g, h) $e_p>e_m$. For $e_p>e_m$: after the particle has become completely detached from the matrix the periphery of the particle is indicated by the dark grey line.

Fig. 4: Analogous to Fig. 3 for the edge-on orientation of the plate-shaped particle, (a, b, e, f) $e_p< e_m$; (c, d, g, h) $e_p>e_m$. Etching is along a longer axis α $(= 69.5a_0)$ of the particle. Image planes: (a-d) $z \equiv 0$ (view along the short axis β), (e-h) $x \equiv 0$ (view along a long axis α).

Fig. 5: Analogous to Fig. 4 for the in-plane orientation of the plate-shaped particle, e_p and e_m are indicated, (a, b) $e_p< e_m$, (c, d) $e_p>e_m$. Etching is along the shorter axis β $(= 9.5a_0)$ of the particle. Image plane: $y \equiv 0$.

Fig. 6: Pseudo-three-dimensional perspective colour presentations of etched particles. The light illuminates the simulated structure from upper left. Golden: particle atoms, blue: matrix atoms. δ is the approximate (± 1) z-coordinate (in units of a_0) of the front of etching (=most advanced point of the solid-etchant interface) and ω is the respective approximate number (in units of 10^6) of steps performed (=number of dissolved atoms). Left column: (a, c, e, g) e_p=1.70 and e_m=2.21, i.e. $e_p<e_m$; the front half of the system has been cut away – through the center of the particle; the area of the cut is smoothly coloured, whereas the solid-etchant interfaces are shown with their actual atomic roughness. Right column: (b, d, f, h) e_p=2.21 and e_m=1.70, i.e. $e_p>e_m$. (a, b) sphere, (note the bottle neck at the top in (a), see also Fig. 3a), (c, d) rounded cube, (e, f) edge-on orientation of the plate, (g, h) in-plane orientation of the plate.

Fig. 7: Effects of varying the energy ratio e_m/e_p, but keeping $e_m \equiv 2.21$ constant, on the etched profile of a spherical particle. e_p, e_m, and e_m/e_p are indicated. For $e_p<e_m$ the front of etching is in the particle and for $e_p>e_m$ it is in the matrix. Image plane: $y \equiv 0$. Two stages of etching are shown: (i) the front of etching has just reached the level $z \approx 0$, i.e. the front is at the level of the original particle center, and (ii) $z \approx 35a_0$, i.e. the front is $\alpha/2$ below the level of the original particle center. α is the particle radius. ω is the respective approximate number (in units of 10^6) of steps performed

Fig. 8: Analogous to Fig. 7. Effects of varying e_p and e_m at constant ratio $e_m/e_p \equiv 1.15$.

Fig. 9: Effects of lacking fresh etchant at the bottom of the etch-pit. The particle is of spherical shape. The presentation is analogous to Fig. 3a. e_p=1.70 and e_m=2.21. The coefficient λ appearing in Eq. (6) is indicated. The front of etching (=most advanced point of the solid-etchant interface) is at $z \approx \delta a_0$. ω is the respective approximate number (in units of 10^6) of steps performed.

Fig. 10: Analogous to Fig. 3(b), but the interactions with atoms in $\mu \leq 3$ coordination shells are allowed for. e_p=1.92 and e_m=2.21. The grey line shows the results for μ=1. The subscripts of ω in the small tables indicate μ. (a) μ=2, i.e. first and second nearest neighbor interactions and (b) μ=3, i.e. first, second, and third nearest neighbor interactions.

Fig. 11: Successive stages of the growth of an in-plane pit by etching. (a-i) Simulated top views along [001]. The solid-etchant interface is shown; golden: particle atoms, blue: matrix atoms. Before the start of etching the top of the plate-like particle is covered by four atomic layers of matrix. Normalized binding energies: e_p=1.70 and e_m=2.21. The dashed white line in (a) outlines the extension of the particle in the plane $z \equiv 0$ before the start of the simulation; length of the longer axis

α: 69.5a_0. (j-l) Actual bright field TEM-images, printed with inverted contrast, of three in-plane γ-pits in $Ni_{69}Co_9Al_{18}Ti_4$. The magnification of (j-l) is the same. The length of the two axes of the γ-pit shown in (l) differ by ±7%.

Table 1: Radius r_j of the j^{th} coordination shell, number c_j of neighbors in the j^{th} coordination shell of an atom in a perfect {001}-, {111}-, and {011}-surface, and normalized (to $k_B T$, T=300K) pair-interaction energies $\varepsilon_{Cu\,j}$ and $\varepsilon_{Ni\,j}$, $1 \le j \le 3$, of Cu and Ni, respectively.

j	r_j/a_0	c_j			$\varepsilon_{Cu\,j}$	$\varepsilon_{Ni\,j}$
		{001}	{111}	{011}		
1	$1/\sqrt{2}$	8	9	7	6.64	8.62
2	1	5	3	4	1.96	1.22
3	$\sqrt{3/2}$	12	15	14	0.27	0.23

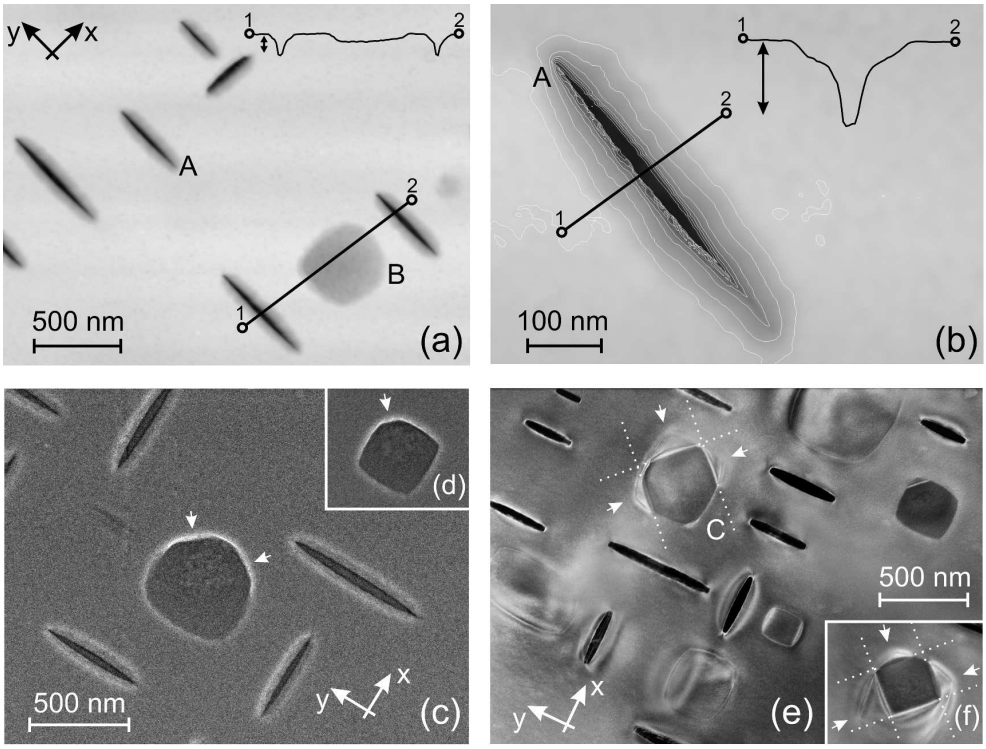

Fig. 1

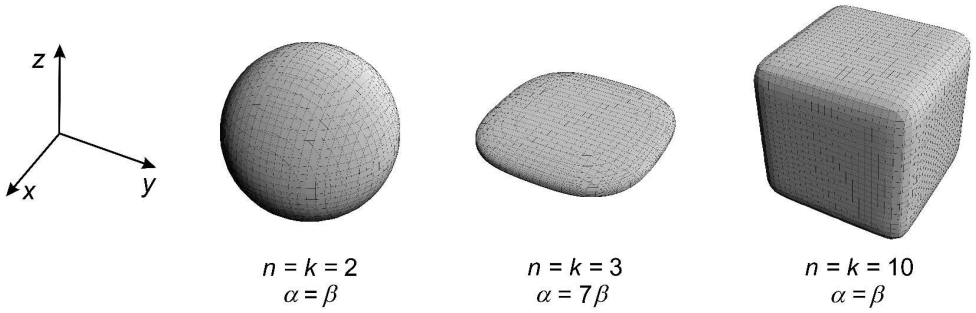

Fig. 2

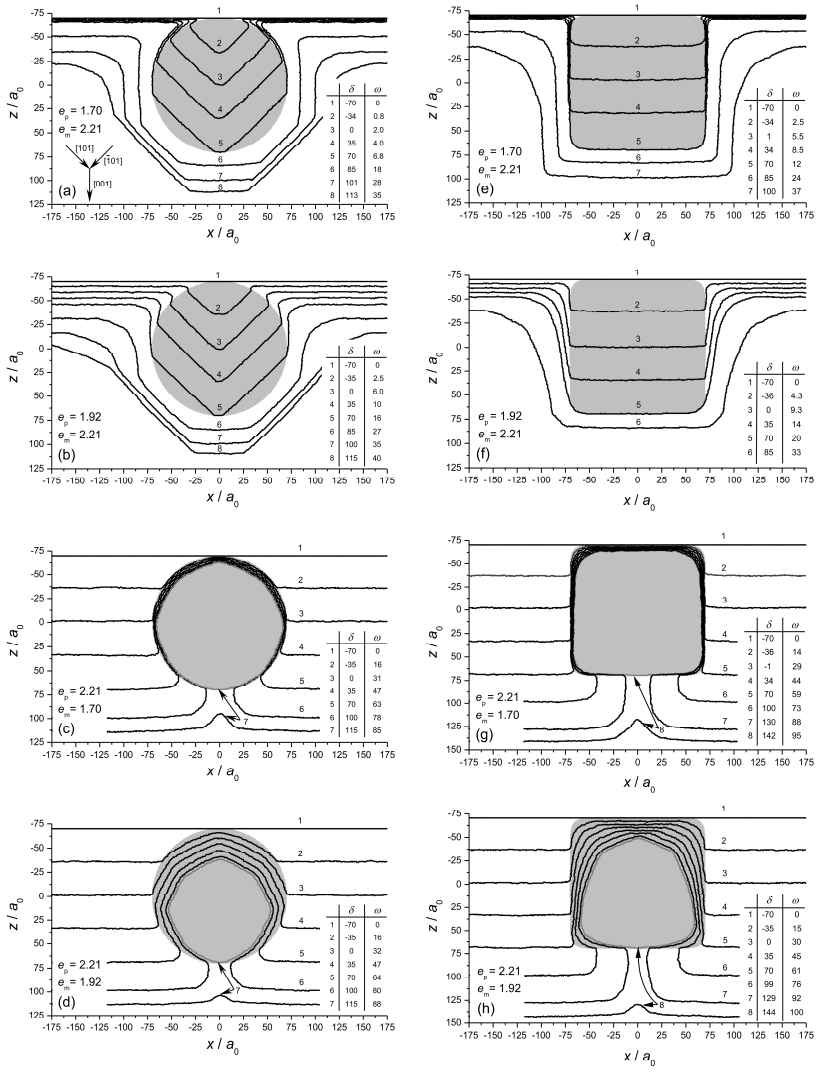
(a)
e_p = 1.70
e_m = 2.21
[101]
[101]
[001]
(b)
e_p = 1.92
e_m = 2.21
(c)
e_p = 2.21
e_m = 1.70
(d)
e_p = 2.21
e_m = 1.92
(e)
e_p = 1.70
e_m = 2.21
(f)
e_p = 1.92
e_m = 2.21
(g)
e_p = 2.21
e_m = 1.70
(h)
e_p = 2.21
e_m = 1.92
z / a_0
x / a_0

Fig. 3

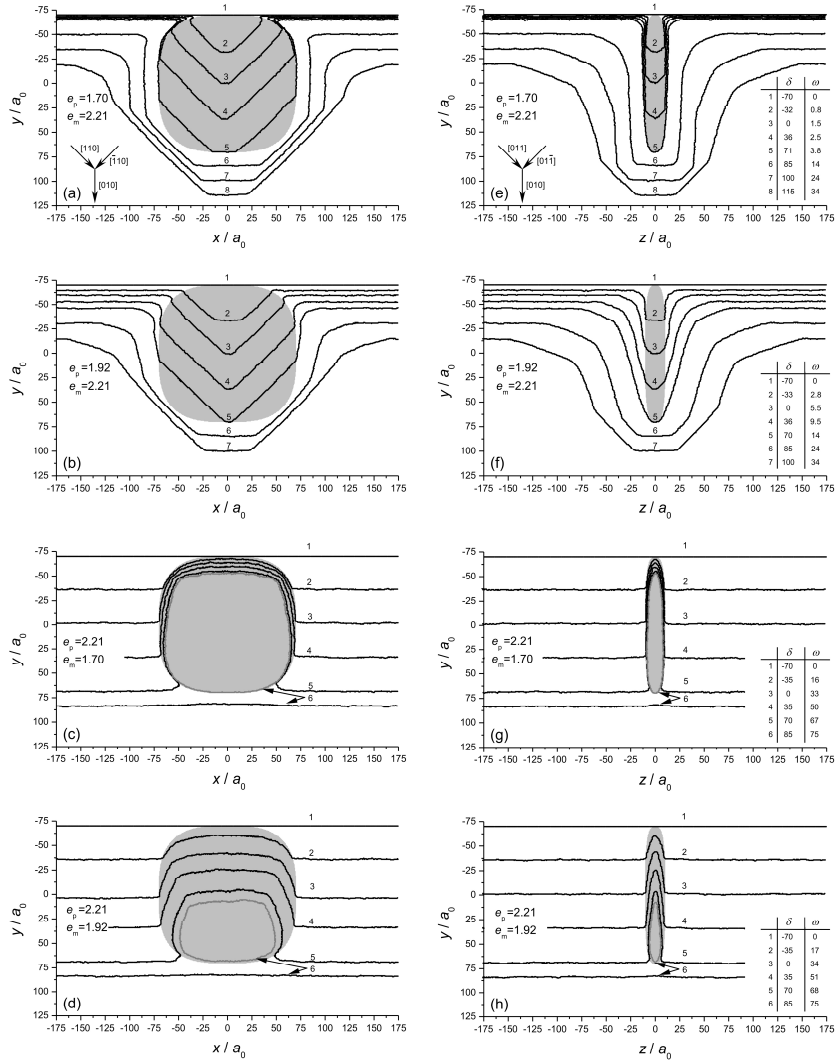

Fig. 4

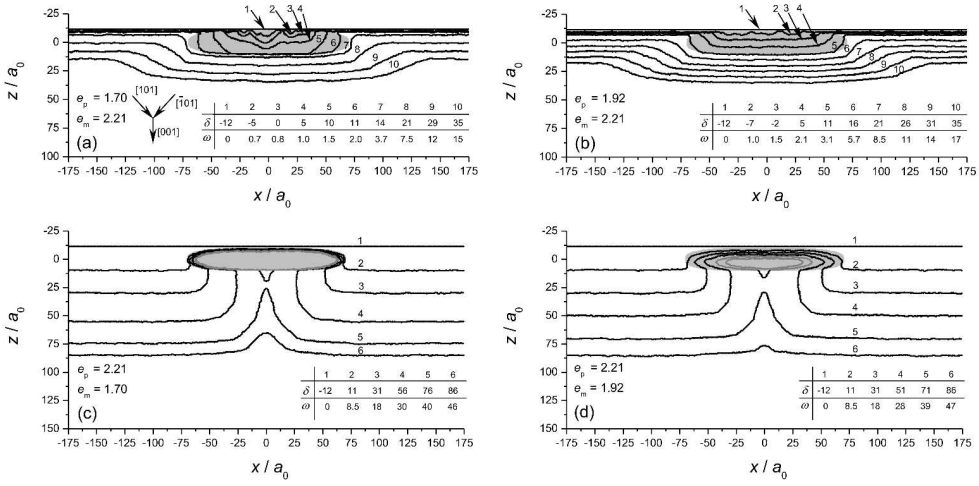

Fig. 5

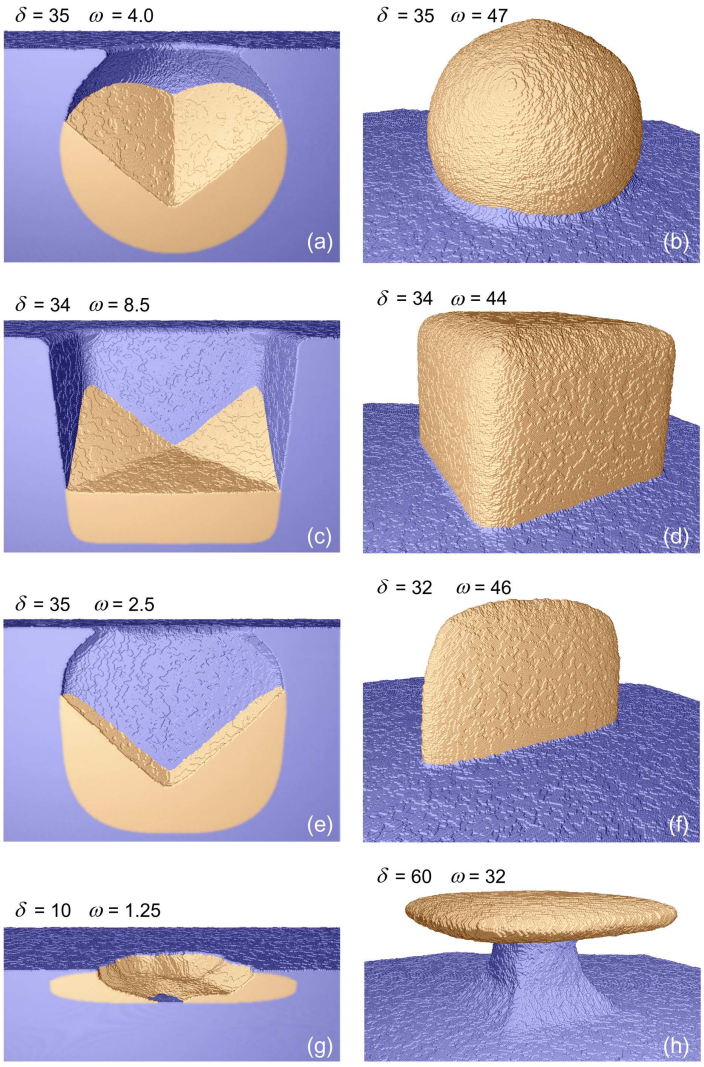
δ = 35 ω = 4.0
(a)
δ = 35 ω = 47
(b)
δ = 34 ω = 8.5
(c)
δ = 34 ω = 44
(d)
δ = 35 ω = 2.5
(e)
δ = 32 ω = 46
(f)
δ = 10 ω = 1.25
(g)
δ = 60 ω = 32
(h)

Fig. 6

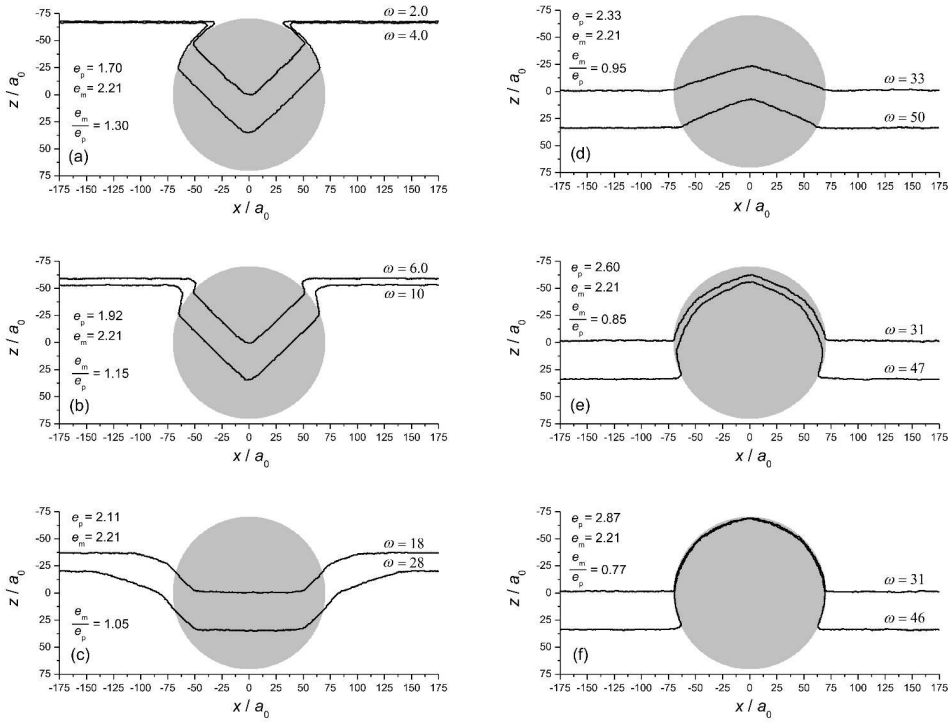

Fig. 7

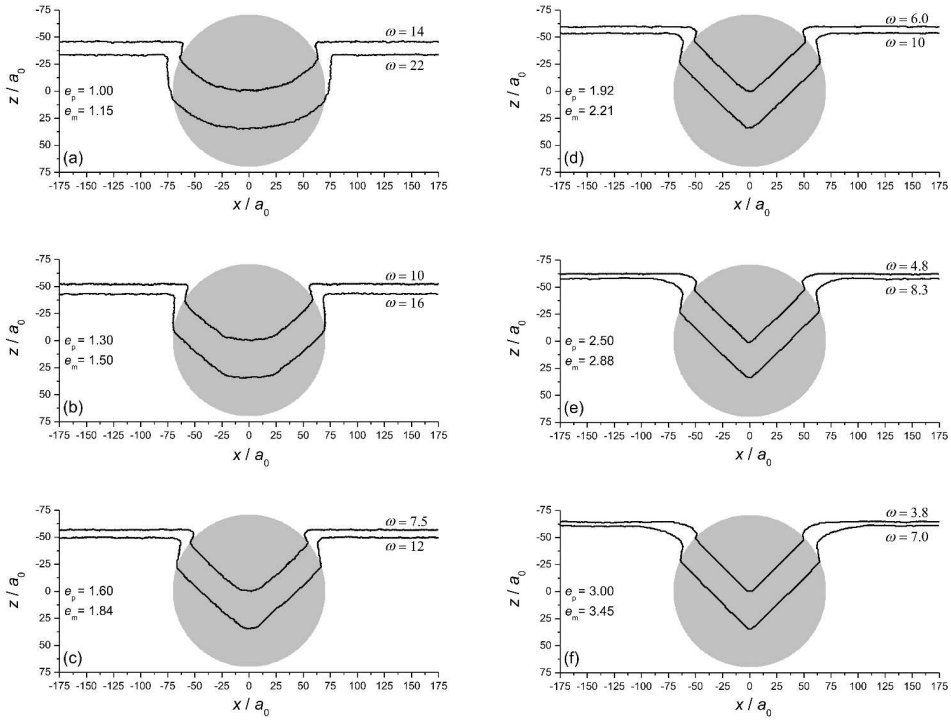

Fig. 8

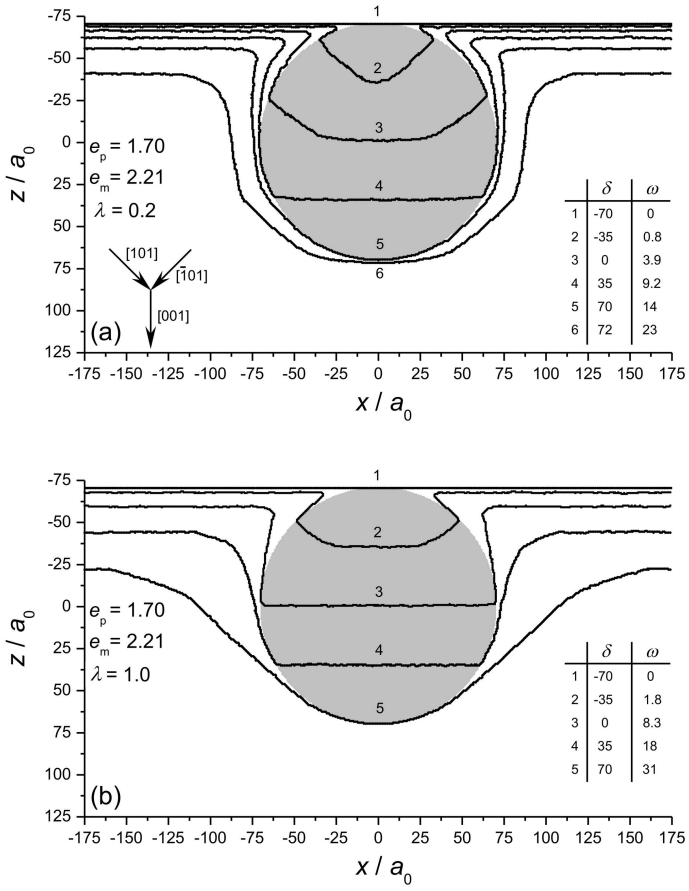
z / a0
x / a0
ep = 1.70
em = 2.21
λ = 0.2
[101]
[$\bar{1}$01]
[001]
(a)
δ ω
1 -70 0
2 -35 0.8
3 0 3.9
4 35 9.2
5 70 14
6 72 23
ep = 1.70
em = 2.21
λ = 1.0
(b)
δ ω
1 -70 0
2 -35 1.8
3 0 8.3
4 35 18
5 70 31

Fig. 9

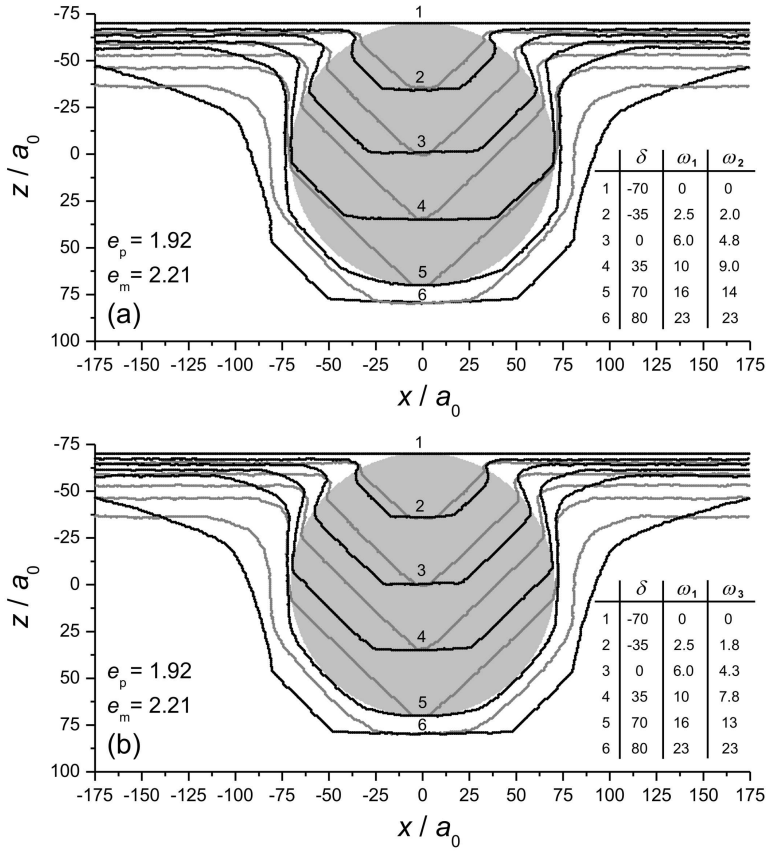
z / a0
x / a0
ep = 1.92
em = 2.21
(a)
(b)
δ ω1 ω2
1 -70 0 0
2 -35 2.5 2.0
3 0 6.0 4.8
4 35 10 9.0
5 70 16 14
6 80 23 23
δ ω1 ω3
1 -70 0 0
2 -35 2.5 1.8
3 0 6.0 4.3
4 35 10 7.8
5 70 16 13
6 80 23 23

Fig. 10

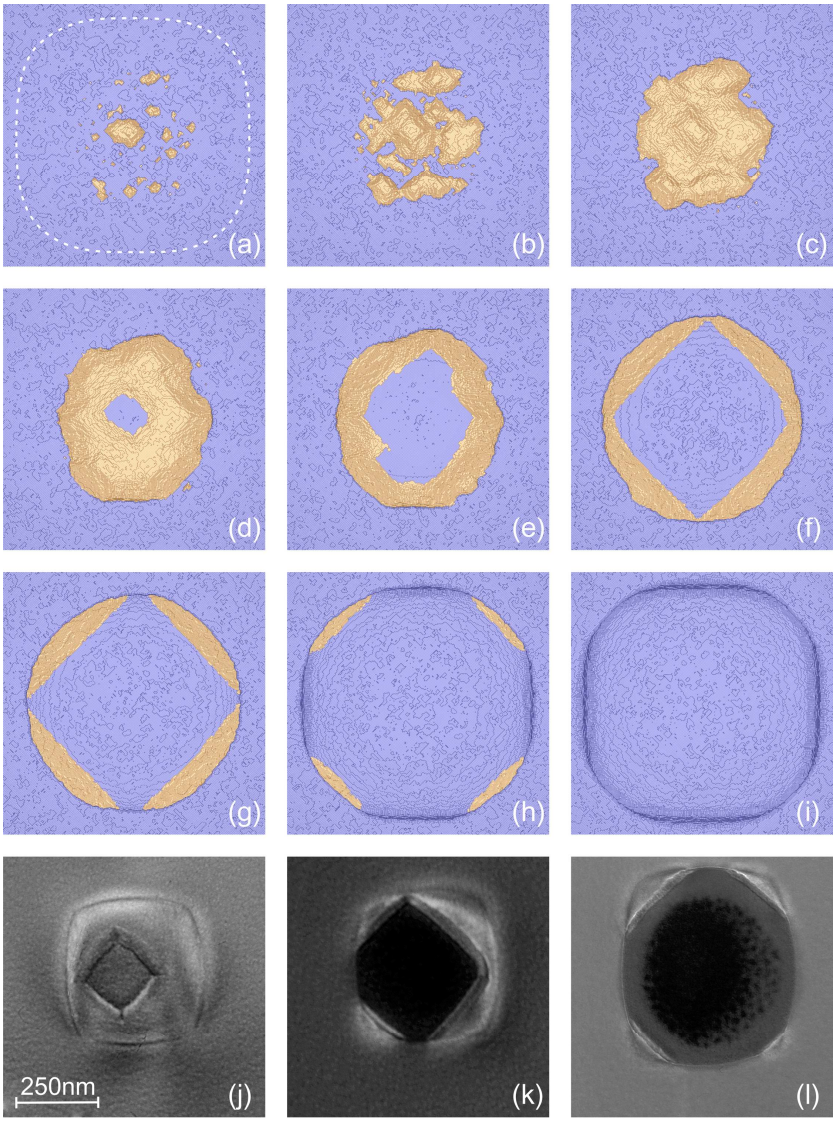

Fig. 11